

Mechanically Tunable Terahertz Metamaterial Perfect Absorber

Lewis K. Piper, H. Johnson Singh, Jonathan R. C. Woods, Kai Sun, Otto L. Muskens, and Vasilis Apostolopoulos*

The development of a wide range of technologies based on terahertz (THz) electromagnetic radiation drives a strong demand for flexible optical elements. Metasurfaces based on metallic resonators offer a versatile toolkit that permits easy tuning over a wide spectral range by the geometric design. Herein, a mechanically tuned metasurface perfect absorber comprised of split-ring resonators in combination with a metallic mirror in a microcavity arrangement, is demonstrated. By mechanically tuning the length of the microcavity in the range of 10 μm and above, precise control over the perfect absorption condition is exhibited. A maximum recorded extinction of 45.8 dB is obtained at the perfect absorption condition, corresponding to a suppression of the reflected radiation by almost five orders of magnitude. Experiments are performed in a reflection arrangement using a terahertz time-domain spectrometer. Simulations of the experimental arrangement show that near-field effects are weak and the enhancement of metamaterial perfect absorption is in agreement with purely interferometric effects.

1. Introduction


Terahertz (THz) technology finds important new applications in fields such as communication, security, and nondestructive testing.^[1–3] Optical elements that are based on refractive index variation and polarization, such as fibers and waveplates, are cumbersome to achieve and mostly inefficient at the long wavelengths of THz waves. Metasurfaces are the ideal platform to create new optical functionalities in the THz range where traditional optical elements are lacking, primarily on account of their ability to create independent custom electric and magnetic responses to incident radiation. As such the development

of new materials and structures for the THz regime to facilitate improved devices and components is the focus of intense research. Specifically, electrodynamic metamaterials and metasurfaces have exhibited unique properties which simply cannot be achieved with conventional materials.^[4–8] Metamolecules based on split-ring resonators (SRRs) have been shown to create THz metamaterials that show a resonant response to incident electromagnetic (EM) waves.^[9–11] By taking advantage of the very high refractive index of metallic structures in the THz spectral region, the response of the metamaterials can be easily scaled geometrically for different wavelengths. Metamaterial concepts have been successfully applied to other parts of the electromagnetic spectrum, including the infrared and visible domains.

An important category of devices using this technology platform is the metamaterial perfect absorbers (MPAs) that have been realized over a significant portion of the EM spectrum.^[12–17] Examples of their applications include light harvesting,^[18] optical sensors,^[19] second-harmonic generation,^[20] negative refractive indices^[21] and thermal black-body control.^[22] Several methods for achieving a perfect absorber based on metasurfaces have been demonstrated, which include the addition of metallic films,^[14] graphene,^[16] multiple metamaterial geometries,^[23] the use of semiconductor structures,^[24] and the inclusion of metamaterials within microcavities.^[25]

Alongside static applications, the possibility of realizing devices with tunable or reconfigurable characteristics is of interest for achieving flexible and agile functionalities. In previous works, electrostatic control of MPAs using microelectromechanical systems (MEMS) has been achieved in the gigahertz (GHz) range by a variety of works.^[26] Lei et al.^[27] furthermore demonstrated a magnetically tunable MPA at GHz frequencies with an absorptivity that reaches 99.2%. Ma et al.^[28] used a nontunable MPA to achieve absorptions near 74% in experimental work characterized by Fourier-transform IR spectroscopy. Liu et al.^[29] achieved fast kilohertz (kHz) modulation of an MPA stack with up to 80% peak absorption. A mechanically tunable air gap was also used by Schalch et al.,^[30] but this research concentrates on much larger air gaps of up to a millimeter, with typical absorptions achieved in the region of 60–80%. In THz time-domain experiments, MEMS-type perfect absorber designs have been demonstrated that were able to continuously tune from the

L. K. Piper, H. J. Singh, J. R. C. Woods, K. Sun, O. L. Muskens, V. Apostolopoulos
Physics Astronomy
Faculty of Engineering and Physical Sciences
University of Southampton
Southampton 243732, UK
E-mail: v.apostolopoulos@soton.ac.uk

 The ORCID identification number(s) for the author(s) of this article can be found under <https://doi.org/10.1002/adpr.202100136>.

© 2021 The Authors. Advanced Photonics Research published by Wiley-VCH GmbH. This is an open access article under the terms of the Creative Commons Attribution License, which permits use, distribution and reproduction in any medium, provided the original work is properly cited.

DOI: 10.1002/adpr.202100136

under- to overcoupled regime^[31,32] by shifting the metasurface resonance frequency. A controllable phased array for beam steering was demonstrated by dynamically shifting the resonance frequency in the MPA using ultrafast free-carrier excitation.^[33]

In this work, we demonstrate a THz MPA that enables precise control over the perfect absorption condition by mechanically tuning the proximity of the metasurface to a mirror ground plane and we demonstrate up to 45.8 dB resonant absorption, which is near the signal-to-noise ratio of our THz spectrometer at 600 GHz. We make use of the essentially independent operating principles of an SRR metasurface and a metal mirror to form an air-filled microcavity with precise control over component separation through the use of a piezoelectric actuator. Our work achieves very high accuracy (± 10 nm) in the control and measurement of the cavity thickness, which is combined with a very high dynamic range of absorption of 45.8 dB, close to the limit of what our THz time-domain spectrometer can measure. The work detailed in this study looks at the effectiveness of manipulating the MPA response and its sensitivity to design parameters, with scope in the future to use them for more efficient THz detection and sensing applications.^[13,34] The system of the THz metamaterial perfect absorber with an SRR metasurface and a metal mirror to form an air-filled microcavity can be used for the detection of gas species in the THz range and refractive index sensing for spectroscopy in the THz range.^[35] Further, we present numerical simulations to explain the mechanism behind the enhanced absorption, which show that near-field effects are negligible at the distances where maximum absorption occurs. Our precisely tunable experimental system is in good agreement with the purely interferometric interpretation of the MPA response.^[36]

2. Experimental Section

Gold SRRs of 45 μm side length and 100 nm thickness were fabricated on a quartz substrate using photolithography. **Figure 1a** shows an optical microscopy image of the SRRs on the quartz substrate. A separate uncoated gold mirror with a surface flatness of 63 nm over a diameter of 12.7 mm was mounted onto a piezoelectric translation stage. The array of SRRs combined with the mirror reflector forms a tunable MPA cavity as shown in **Figure 1b**, which shows the experimental arrangement of the cavity. The separation of the gold mirror to the SRRs was controlled with 10 ± 0.6 nm precision using a closed-loop piezoelectric stage.

Terahertz time-domain spectroscopy was used in a reflection configuration to measure the response of the SRRs coupled to a reflecting microcavity. **Figure 1c** shows the experimental setup for the time-domain THz spectrometer, which was combined with a white-light interferometer setup for calibration of the cavity thickness. The THz time-domain reflectivity part of the setup was based on a commercial system (Mini Z, Zomega Terahertz Corporation) containing an ultrafast pulsed laser which generates THz using a photoconductive antenna (PCA), while the measurement of the THz pulse was achieved using a ZnTe Pockels effect detection system based on a polarizing prism with balanced photodiodes.

A separate visible-range white light interferometer was used to establish parallelism of the surfaces and to calibrate the cavity thickness. Initially, the collimated output from a supercontinuum light source (Fianium) was used as the broadband source, and reflected light over a wavelength range from 600 to 800 nm was analyzed using a spectrometer (Ocean Optics). The spacing

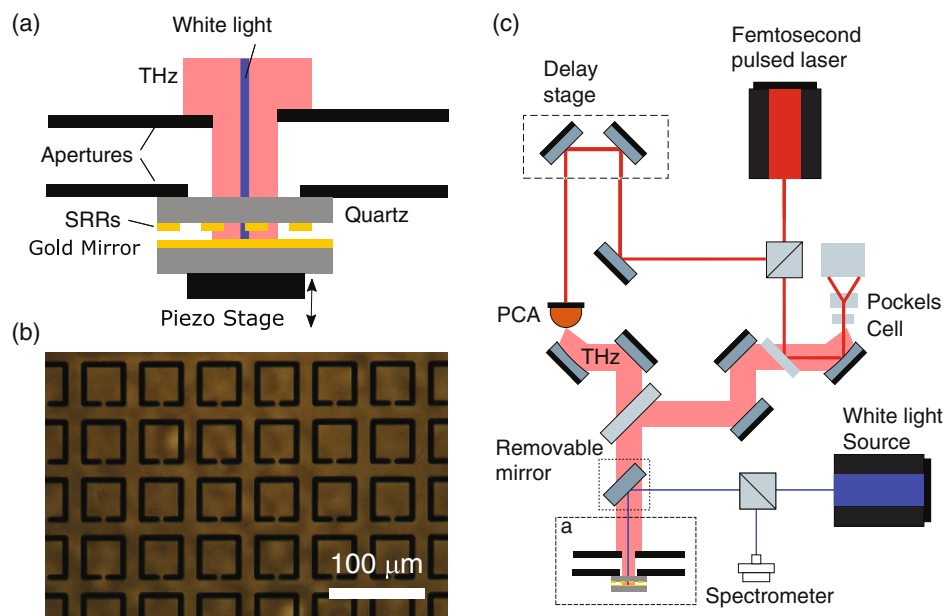


Figure 1. Experimental configuration. a) Microcavity configuration containing the SRR array in proximity to a gold mirror mounted on a closed-loop piezo stage. Two apertures are used to suppress spurious THz back reflections from the sample holder. b) Optical microscope image of 45 μm gold SRRs on quartz substrate. c) Experimental setup for time-domain THz reflectivity measurements and white-light interferometry of cavity thickness, showing the photoconductive antenna (PCA), scanning delay stage, and silicon beam splitter.

of the etalon fringes was used to extract the cavity thickness at each data point before a THz experiment was conducted. The visible light beam was coupled into the beam path using a removable mirror on a magnetic stand, and the mirror was removed out of the THz beam path after each calibration step.

The THz radiation was collimated and directed toward the cavity using gold parabolic mirrors. A 5 mm thick silicon wafer was used as a beam splitter to direct the reflected THz radiation to the THz detection system. In the analysis of time-domain THz reflectivity signals, the presence of unwanted reflections from different parts of the setup is a particular problem that can complicate further analysis. Therefore, appropriate effort was made to reduce reflections in a time window around the primary reflection signal. Suppression of a number of unwanted THz back reflections from edges of the sample holder was achieved with the use of two 10 mm diameter apertures placed in front of the SRR on quartz sample, as shown in Figure 1a. Furthermore, the silicon beam splitter thickness of 5 mm was chosen so that delayed pulses caused by the multiple reflections of the beam splitter were spaced far enough apart and attenuated sufficiently so as to prevent overlap with the pulse being measured. By Fourier transforming the time-domain response of the THz signal over a selected time window, the THz frequency domain spectrum of the MPA sample was measured for different cavity thicknesses. The signal was normalized to a reference THz time-domain scan, for which the MPA was used at a cavity thickness of 50 μm . At this cavity thickness the spectral response is flat as the cavity spacing approaches half the wavelength, resulting in a node of the THz electric field at the location of the SRRs, and therefore, the effect of the SRRs in the spectrum is at a minimum. This method was found to provide much better results than other reference methods, such as replacing the SRR on quartz sample by a plain quartz substrate, due to small uncontrolled variations in optical thickness which have a large effect on the normalization process.

Numerical simulations were conducted using COMSOL Multiphysics 5.4. Full-field formalism was adopted with periodic boundary conditions (Floquet) applied on all four sides of the computational geometry assuming an infinite 2D periodic structure in the x - y plane. The SRR was positioned at the center of the computational window with a semi-infinite quartz substrate. The refractive index of the quartz substrate in the THz regime was experimentally measured and was taken to be $n_{\text{subs}} = 2.0$, while that of the Au SRR and mirror plate were extracted using a Drude model as reported in the literature.^[37] The cavity system was assumed to be embedded in air medium and the relative permeability was taken to be $\mu_r = 1$. Port conditions were implemented for launching the incident beam, which was assumed to be a plane wave, linearly polarized (LP), propagating from the SRR side toward the mirror plate, i.e., along the z -direction. Reflectance (R) and transmittance (T) were extracted using S -parameters and absorbance (A) was calculated using the relation, $A + R + T = 1$.

3. Results

Figure 2 shows the experimental and simulated response of the tunable SRR-mirror cavity. Corresponding color maps of

reflectivity against frequency and cavity thickness are shown in Figure 3. Experimental reflectivity spectra for the tunable SRR-mirror cavity are shown in Figure 2a,b for different values of the cavity thickness between 10 and 45 μm , where the two data-sets correspond to different experimental runs which are respectively labeled as Experiment 1 and 2. Experiments 1 and 2 are identical experiments using the same SRR on quartz sample and gold mirror but performed with complete realignment of the setup and on different days. Corresponding simulation results for the same SRR and cavity dimensions are shown in Figure 2c. The power spectrum of the reflected THz signal is highly dependant on the separation between the SRRs and the gold mirror, and shows a sharp resonant drop around the optimal MPA configuration. Figure 2a shows a drop in the reflectivity of 34 dB, which occurs at a cavity thickness of 19 μm , while Figure 2b has a drop in reflectivity of 45.8 dB, which occurs at a cavity thickness of 18.4 μm . The minima in the reflected THz signal occur at 575.6 and 591 GHz respectively in the two experiments. In comparison, the simulations that use finite element modeling in Figure 2c show a drop in reflectivity of 66.7 dB at 561.1 GHz.

Figure 2d shows the spectral position of the dip in spectral reflectivity for each experiment at different cavity thicknesses, normalized to the frequency scan of the minimum MPA reflectivity. The observed shift in the frequency is around $\pm 5\%$ of the center frequency, or around 50 GHz, which is somewhat smaller for the experimental results compared to that of the simulation. Figure 2e,f shows the amplitude of the minimum reflectivity of the cavity at different cavity lengths on linear (e) and logarithmic (f) axes. These respectively display that the reflectivity in the experimental results is more susceptible to the cavity thickness than that of the simulated results, and also that the critical thickness of the simulated cavity is smaller than that of the experiment.

Figure 4 shows the corresponding phase response of the reflected THz for the two experimental cavities as well as the simulations. Correspondingly, Figure 5 shows in more detail the relationship between the phase of the reflected THz from the microcavity for different cavity thicknesses in the range 10–20 μm . The simulated response, shown in Figure 4c and 5c, shows the expected behavior for the hybrid SRR-microcavity structure. For cavity thickness sufficiently far (i.e., several μm) from the critical thickness, we see a slow evolution of the phase over the spectrum from 0 to 2π , which is indicative of the individual SRR resonance. As the cavity approaches the critical thickness, an additional sharp phase jump becomes apparent, related to the interplay of the metasurface and cavity modes. Cavity sizes smaller than that of the critical thickness display a relative increase of the phase to 2π , while cavity sizes larger than the critical thickness show a jump back to zero phase. As a result, the phase response splits up in two separate regions for thicknesses below and above the critical thickness, where the phase flips to either 2π or 0 above the perfect absorption frequency. Qualitatively the same behavior for the MPA structure, including the characteristic splitting of phase response, is found in the experimental data of Figure 4a,b. Differences in the slow overall phase evolution are attributed to the normalization to the reference spectrum between experiments and theory, where in the latter case we normalized to the substrate without SRRs

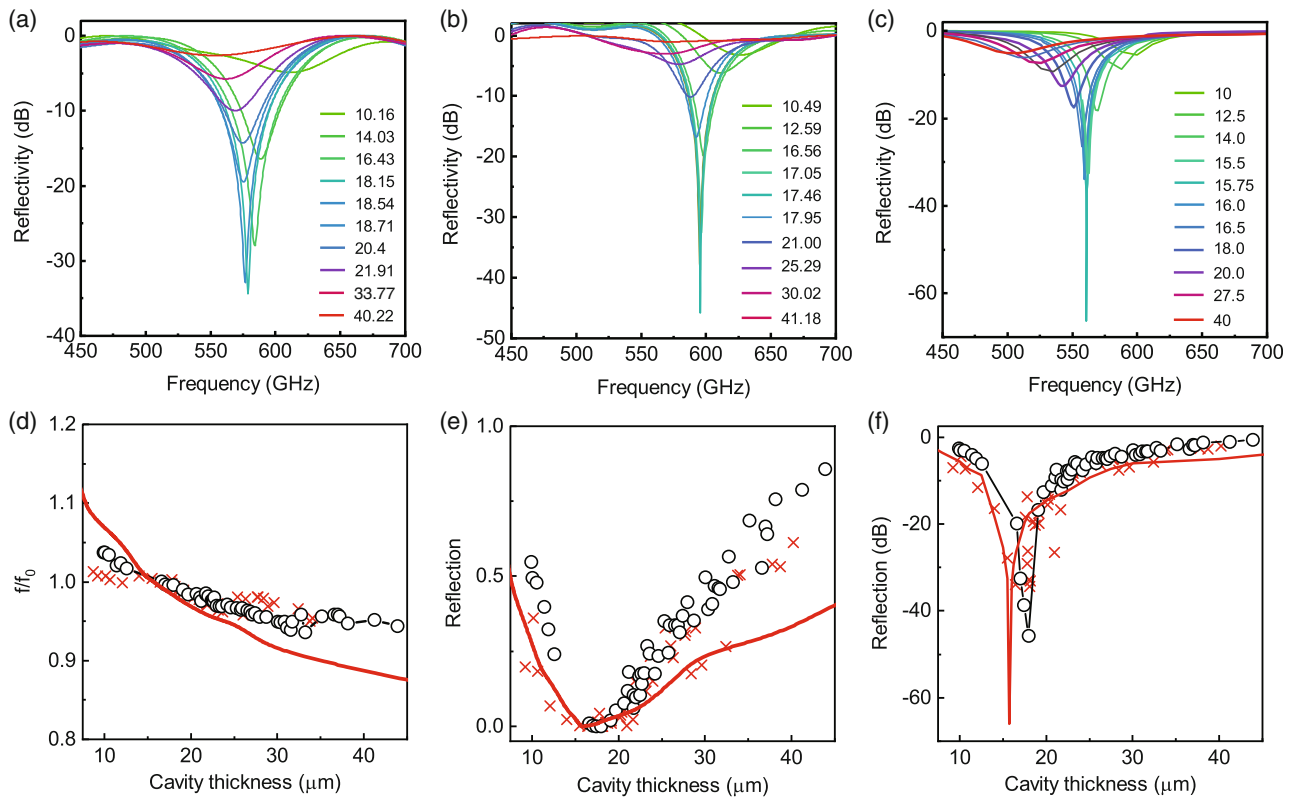


Figure 2. a–c) Terahertz reflectivity spectra for different values of cavity size. a, b) Experimental traces and c) simulated spectral response of the meta-material for a range of cavity thicknesses, from 10 to 41.2 μm , as shown in the legend. d–f) Extracted values for resonance frequency normalized to the perfect absorption frequency f_0 (d), minimum in reflectivity on linear scale (e) and log scale (f), as a function of the cavity thickness. Data shown for the two experimental runs (crosses, dots) and simulations (red line).

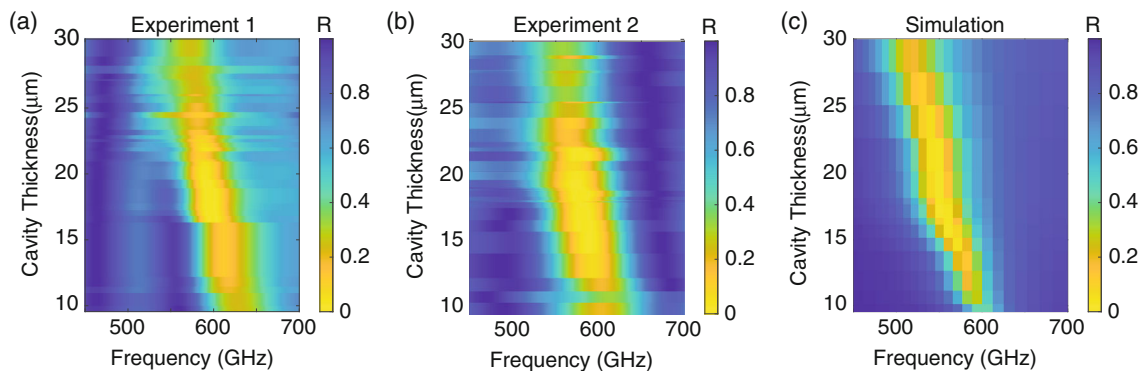


Figure 3. Figure showing the effect of changing cavity thickness on the reflectivity of the metasurface. a–c) Maps of the reflected THz spectrum versus cavity thickness, for experiments 1 and 2 (a, b) and for simulations (c).

and subtracted a slowly varying background phase taken at 50 μm cavity length. This deviation does not affect significantly the fast phase evolution around the cavity critical condition.

The maps in Figure 5 clearly show the presence of a phase singularity at the perfect absorption location where the optical vortex results in a phase accumulation of 2π . The point in the center of the phase vortex occurs at the critical cavity thickness, which in turn corresponds to the minimum signal of the reflected THz response.

4. Discussion

We have shown in the previous section that the phase and resonant position of SRRs can be manipulated through precise control of the separation of the SRR and a parallel gold mirror. These shifts are due to the destructive interference of the THz radiation that passes through the cavity with the THz radiation that is reflected by the SRRs. Because the phase shift induced by the cavity will vary for each wavelength of the THz, the wavelengths

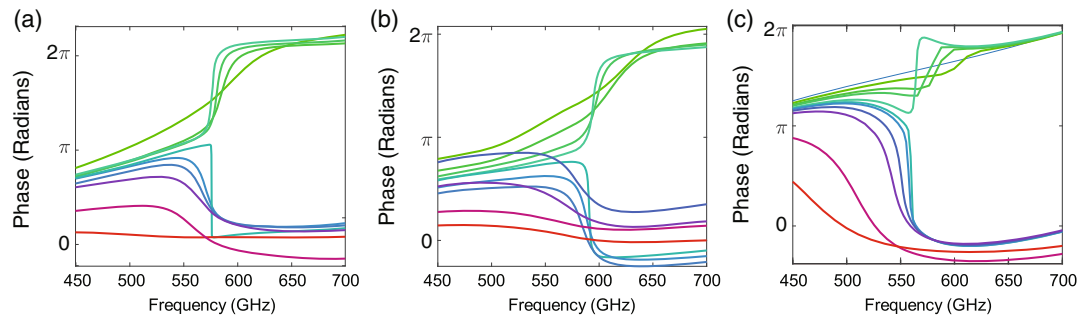


Figure 4. Figures showing the a,b) experimental and c) simulated phase response of the metamaterial for the same range of thicknesses as Figure 2.

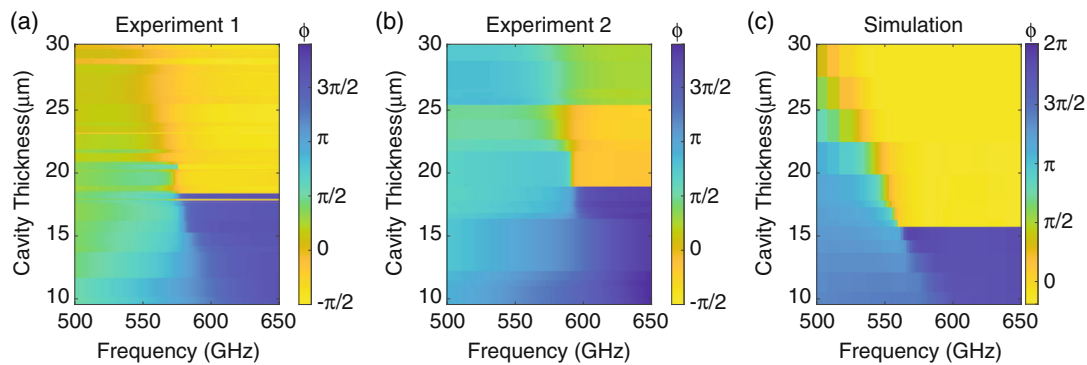


Figure 5. Figure showing the effect of changing cavity thickness on the relative phase of the metasurface and the corresponding shift in the sign of the phase. a–c) Maps of the phase from the reflected THz spectrum versus cavity thickness, for experiments 1 and 2 (a,b) and for simulations (c).

that exhibit the strongest destructive interference will shift with the cavity length. An analytical cavity model was presented by Chen^[36] that quantitatively explains this behavior using only far-field interference. Subsequently, we investigate the validity of this approach under the conditions of our experiment.

Using finite element modeling and refractive index data from Ordal et al.,^[37] we numerically calculate the resonances of a single isolated SRR. For calculating the scattering and absorption cross-sections of individual isolated SRRs, the scattered field formalism was adopted. We used a spherical PML of thickness 100 μm surrounding the model geometry. The PML was placed a half wavelength away from the SRR. The entire structure was divided into domains and subdomains, and each domain was meshed using free tetrahedral meshing of maximum element size 6 elements per wavelength outside the SRR and extremely fine meshing for the SRR. We adopt a direct solver to solve the wave equation, such as to calculate the cross-sections for both linear (plane wave) polarizations parallel and perpendicular to the split-ring gap. A sweep parameter was used to scan the wavelength range from 0.5 to 5 THz. **Figure 6a** shows the resonances of the isolated SRR, which occur under two perpendicular polarizations of incident THz radiation. The first and third resonances of the SRR occur when the incident electric field is polarized across the gap and the second resonance occurs when the polarization is perpendicular to the gap.^[9,38] The resonances that occur under parallel polarization are typically narrower than the resonance under perpendicular polarization. This work

focuses on the first resonance, as the third resonance is far weaker and could not be clearly observed in our experimental arrangement. **Figure 6b** shows the corresponding electric (E)-field, charge distribution, and current of the SRRs for each resonance. The collection of charge on opposite sides of the gap in the SRR manifests as the capacitance of the SRR and hence the electric response, while the currents represent the magnetic inductance of the SRR. **Figure 6c** gives a breakdown of the first resonance into the corresponding electric and magnetic responses of the resonator. It is seen that the resonance has strong contributions from both the electric and magnetic responses.

Following our basic understanding of the isolated single SRR, we can investigate the response of an array of SRRs coupled to the cavity, as shown in **Figure 7**. To investigate the dependence of the spectral response on cavity thickness, we first look at the near field and induced charge plots of the cavity. **Figure 7a** shows the arrangement of the cavity formed between the gold mirror and the array of SRRs. By probing the magnitude of the electric near field at multiple distances z from the SRRs as indicated by the cross-section planes, the vertical extent of the near field can be determined. **Figure 7b** shows the near field ($|E/E_0|$) at a frequency of 0.624 THz, for different planes z distance away from the surface of the metamaterial layer within the 16.5 μm cavity. The near field is seen to be mostly confined very close to the SRR and becomes vanishingly small at a separation of 10 μm or more, suggesting negligible near-field interaction between the SRRs and the cavity plate. The vanishing of the near field confirms that

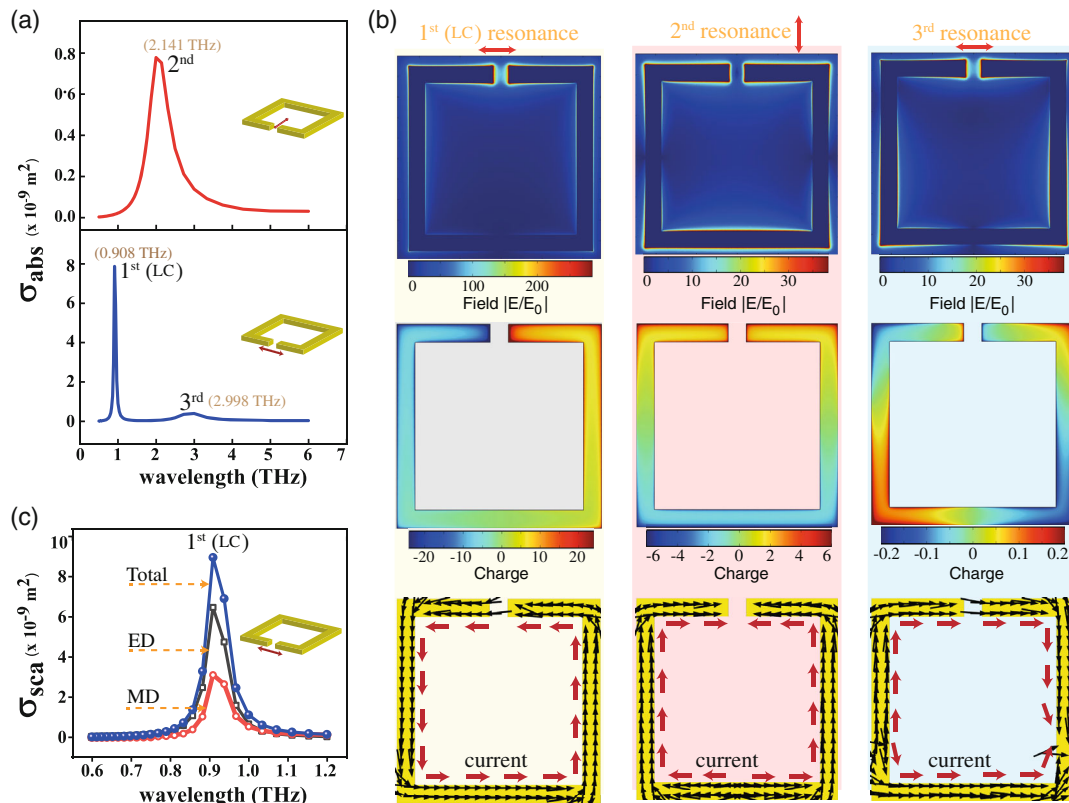


Figure 6. Numerical simulations for a single isolated SRR. a) Absorption cross-section for two polarizations of the incident EM wave for electric fields perpendicular and parallel to the gap. b) Near field, charge density, and current distribution for the three main modes. c) Breakdown of the scattering cross-section of the SRR into electric dipole (ED) and magnetic dipole (MD) components.

the maximum absorption enhancement which occurs for larger cavity separation is not related to near-field interactions between the SRRs and the cavity.

The range of cavity thicknesses for which the induced surface charge is non-negligible is further investigated in Figure 7c, which shows the induced charge within the gold mirror by the charge distribution within the SRR at resonance for multiple separations of the SRR and gold mirror. At larger cavity sizes the charge induced by the SRR within the gold becomes significantly curtailed. Figure 7d shows the absorbance of the SRR at different separations of the gold back reflector and the SRRs following the same separations shown in Figure 7c. The top scan at a separation of 16.5 μm in Figure 7d shows the comparison of the SRR absorption with and without the gold back reflector. At 16.5 μm the absorption of the SRRs with the gold is both stronger and over a narrower frequency band than that of the SRR without the gold; the presence of the gold shifts also its absorption peak to a lower frequency. Additionally, when the two layers are brought closer together, such that the induced charge becomes significant, the amplitude of the absorption decreases by up to a factor of 100, and the position of the peak absorption also shifts toward higher frequencies. This is because as the distance decreases the wavelength where the reflected wave off the SRR and the reflected wave off the metal plate are in destructive interference decreases. In all of these cases, the bandwidth of the absorption of the SRR with the back reflector lies within the

bandwidth of the SRR without the back reflector. These two sets of the simulated SRR cavities indicate that the interaction between the gold back reflector and SRR metamaterial is not due to charge induction or charge mirroring at the frequency of the perfect absorption.

5. Conclusion

In conclusion, we have demonstrated THz devices with tunable and reconfigurable characteristics based on a metasurface perfect absorber geometry with mechanically controlled cavity. Our experiment achieves a reflectivity minimum of -45.8 dB close to the detection limit of our THz time-domain setup. The combination of a bidirectional accuracy of $\pm 10 \text{ nm}$ and in situ characterization using a white-light interferometer offers reliable calibration of cavity thicknesses. We show with numerical simulations that the mechanism explaining the enhanced absorption cannot be near-field effects; they are shown to be negligible at the distances where maximum absorption occurs. Our precisely tunable experimental system is in good agreement with the purely interferometric interpretation of the MPA response.^[36] The work demonstrated in this study shows the effectiveness of manipulating the MPA response and its sensitivity to design parameters. This work can be used for more efficient THz detection and sensing applications.^[13,34] Also, in future, the SRR response

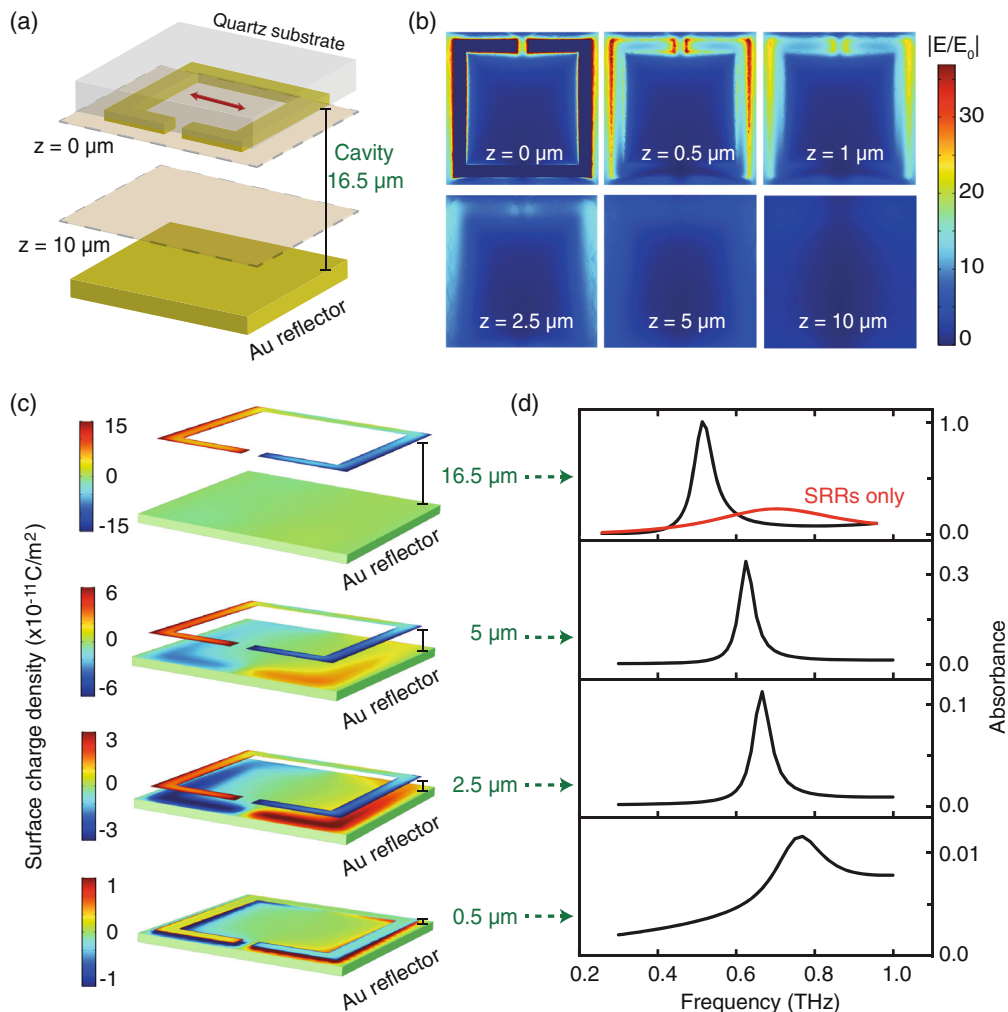


Figure 7. a) Schematic of the metamaterial structure showing a single SRR unit cell on quartz substrate and Au back reflector separated by cavity thickness of 16.5 μm. b) Near-field magnitude $|E/E_0|$ at different planes along the z-direction for the cavity thickness of 16.5 μm at the resonance position of 0.624 THz. For clarity, the field values are scaled down by a factor of 5. Also shown is the schematic of the cavity system with different planes and light polarization direction. b) Surface charge density (in the units of $10^{-11} \text{ C m}^{-2}$) plot for various cavity thicknesses at the corresponding resonance positions. Also shown are the corresponding absorption spectra.

may be tuned using active substrates such as photoconductive insulators,^[39] in addition to more advanced control over the cavity length using, for example, arrays of microelectromechanical piston actuators^[40] to further optimize the maximum absorption and tunability range of the system with potential applications in active phase control.

Acknowledgements

Engineering and Physical Science Research Council (EP/M009122/1, EP/T001046/1). HJS is supported by the Leverhulme Trust through Grant RPG-2018-251.

Conflict of Interest

The authors declare no conflict of interest.

Data Availability Statement

Data associated with this work are available from <https://doi.org/10.5258/SOTON/D1888>.

Keywords

metamaterials, microcavity, perfect absorbers, terahertz, tunable

Received: May 18, 2021
Revised: August 1, 2021
Published online: October 5, 2021

- [1] K.-C. Huang, Z. Wang, *IEEE Microw. Mag.* **2011**, *12*, 108.
[2] M. C. Kemp, P. F. Taday, B. E. Cole, J. A. Cluff, A. J. Fitzgerald, W. R. Tribe, *Proc. SPIE* **2003**, *5070*, 44.

- [3] P. Siegel, *IEEE Trans. Micro. Theory Tech.* **2004**, *52*, 2438.
- [4] C. M. Soukoulis, S. Linden, M. Wegener, *Science* **2007**, *315*, 47.
- [5] H.-T. Chen, A. J. Taylor, N. Yu, *Rep. Prog. Phys.* **2016**, *79*, 076401.
- [6] S. Lee, S. Baek, T.-T. Kim, H. Cho, S. Lee, J.-H. Kang, B. Min, *Adv. Mater.* **2020**, *32*, 2000250.
- [7] Q. Ma, T. J. Cui, *PhotonIX* **2020**, *1*, 1.
- [8] X. Lin, Y. Rivenson, N. T. Yardimci, M. Veli, Y. Luo, M. Jarrahi, A. Ozcan, *Science* **2018**, *361*, 1004.
- [9] W. J. Padilla, A. J. Taylor, C. Highstrete, M. Lee, R. D. Averitt, *Phys. Rev. Lett.* **2006**, *96*, 107401.
- [10] S.-Y. Chiam, R. Singh, C. Rockstuhl, F. Lederer, W. Zhang, A. A. Bettiol, *Phys. Rev. B* **2009**, *80*, 153103.
- [11] C. Rockstuhl, T. Zentgraf, H. Guo, N. Liu, C. Etrich, I. Loa, K. Syassen, J. Kuhl, F. Lederer, H. Giessen, *Appl. Phys. B* **2006**, *84*, 219.
- [12] C. M. Watts, X. Liu, W. J. Padilla, *Adv. Mater.* **2012**, *24*, OP98.
- [13] Y. Yao, R. Shankar, M. A. Kats, Y. Song, J. Kong, M. Loncar, F. Capasso, *Nano Lett.* **2014**, *14*, 6526.
- [14] N. I. Landy, S. Sajuyigbe, J. J. Mock, D. R. Smith, W. J. Padilla, *Phys. Rev. Lett.* **2008**, *100*, 207402.
- [15] J. A. Bossard, L. Lin, S. Yun, L. Liu, D. H. Werner, T. S. Mayer, *ACS Nano* **2014**, *8*, 1517.
- [16] O. Balci, N. Kakenov, E. Karademir, S. Balci, S. Cakmakyapan, E. O. Polat, H. Caglayan, E. Ozbay, C. Kocabas, *Sci. Adv.* **2018**, *4*, eaao1749.
- [17] M. A. Kats, D. Sharma, J. Lin, P. Genevet, R. Blanchard, Z. Yang, M. M. Qazilbash, D. N. Basov, S. Ramanathan, F. Capasso, *Appl. Phys. Lett.* **2012**, *101*, 221101.
- [18] K. Aydin, V. E. Ferry, R. M. Briggs, H. A. Atwater, *Nat. Commun.* **2011**, *2*, 517.
- [19] A. Tittl, P. Mai, R. Taubert, D. Dregely, N. Liu, H. Giessen, *Nano Lett.* **2011**, *11*, 4366.
- [20] J. T. Collins, D. C. Hooper, A. G. Mark, C. Kuppe, V. K. Valev, *ACS Nano* **2018**, *12*, 8.
- [21] E. Plum, J. Zhou, J. Dong, V. A. Fedotov, T. Koschny, C. M. Soukoulis, N. I. Zheludev, *Phys. Rev. B* **2009**, *79*, 035407.
- [22] K. Sun, C. A. Riedel, Y. Wang, A. Urbani, M. Simeoni, S. Mengali, M. Zalkovskij, B. Bilenberg, C. H. de Groot, O. L. Muskens, *ACS Photonics* **2018**, *5*, 495.
- [23] C. Hu, L. Liu, Z. Zhao, X. Chen, X. Luo, *Opt. Express* **2009**, *17*, 16745.
- [24] A. Rifat, M. Rahmani, L. Xu, A. Miroshnichenko, *Materials* **2018**, *11*, 1091.
- [25] K. Bhattarai, S. Silva, K. Song, A. Urbas, S. J. Lee, Z. Ku, J. Zhou, *Sci. Rep.* **2017**, *7*, 10569.
- [26] F. Zhang, S. Feng, K. Qiu, Z. Liu, Y. Fan, W. Zhang, Q. Zhao, J. Zhou, *Appl. Phys. Lett.* **2015**, *106*, 091907.
- [27] M. Lei, N. Feng, Q. Wang, Y. Hao, S. Huang, K. Bi, *J. Appl. Phys.* **2016**, *119*, 24.
- [28] Y. Ma, Q. Chen, J. Grant, S. C. Saha, A. Khalid, D. R. S. Cumming, *Opt. Lett.* **2011**, *36*, 945.
- [29] M. Liu, M. Susli, D. Silva, G. Putrino, H. Kala, S. Fan, M. Cole, L. Faraone, V. P. Wallace, W. J. Padilla, D. A. Powell, I. V. Shadrivov, M. Martyniuk, *Microsyst. Nanoeng.* **2017**, *3*, 17033.
- [30] J. Schalch, G. Duan, X. Zhao, X. Zhang, R. D. Averitt, *Appl. Phys. Lett.* **2018**, *113*, 061113.
- [31] L. Cong, P. Pitchappa, C. Lee, R. Singh, *Adv. Mater.* **2017**, *29*, 1700733.
- [32] L. Cong, P. Pitchappa, Y. Wu, L. Ke, C. Lee, N. Singh, H. Yang, R. Singh, *Adv. Opt. Mater.* **2017**, *5*, 1600716.
- [33] L. Cong, R. Singh, *Adv. Mater.* **2020**, *32*, 2001418.
- [34] L. Cong, S. Tan, R. Yahiaoui, F. Yan, W. Zhang, R. Singh, *Appl. Phys. Lett.* **2015**, *106*, 031107.
- [35] G. Duan, J. Schalch, X. Zhao, J. Zhang, R. D. Averitt, X. Zhang, in *19th Int. Conf. Solid-State Sensors, Actuators and Microsystems (TRANSDUCERS)*, Kaohsiung Taiwan, IEEE, **2017**, pp. 1999–2002.
- [36] H.-T. Chen, *Opt. Express* **2012**, *20*, 7165.
- [37] M. A. Ordal, L. L. Long, R. J. Bell, S. E. Bell, R. R. Bell, R. W. Alexander, C. A. Ward, *Appl. Opt.* **1983**, *22*, 1099.
- [38] S. Linden, C. Enkrich, M. Wegener, J. Zhou, T. Koschny, C. M. Soukoulis, *Science* **2004**, *306*, 1351.
- [39] J. Gorecki, L. Piper, A. Noual, S. Mailis, N. Papisimakis, V. Apostolopoulos, *ACS Appl. Nano Mater.* **2020**, *3*, 9494.
- [40] T. Bifano, *Nat. Photon.* **2011**, *5*, 21.